Achieving simultaneously improved tensile strength and ductility of a nano-TiB 2 /AlSi10Mg composite produced by cold spray additive manufacturing

Xinliang Xie, Chaoyue Chen, Zhe Chen, Wen Wang, Gang Ji, Hanlin Liao

Achieving simultaneously improved tensile strength and ductility of a nano-TiB_2/AlSi10Mg composite produced by cold spray additive manufacturing

Xinliang Xie[1,2*], Chaoyue Chen[3], Zhe Chen[4], Wen Wang[5], Yan Wang[5], Gang Ji[2*], Hanlin Liao[1]

1. ICB UMR 6303, CNRS, Univ. Bourgogne Franche-Comté, UTBM, F-90010 Belfort, France
2. Univ. Lille, CNRS, INRAE, Centrale Lille, UMR 8207 - UMET - Unité Matériaux et Transformations, F-59000 Lille, France
3. State Key Laboratory of Advanced Special Steels, School of Materials Science and Engineering, Shanghai University, Shanghai 200444, China
4. State Key Laboratory of Metal Matrix Composites, Shanghai Jiao Tong University, Shanghai 200240, China
5. School of Metallurgical Engineering, Xi'an University of Architecture and Technology, Xi'an 710055, China

*Corresponding author: Dr. Xinliang XIE (xlxie1990@gmail.com); Dr. Gang JI (gang.ji@univ-lille.fr)

Abstract: The premature failure of components due to poor inter-particle bonding is the most critical issue in cold spray (CS) additive manufacturing. Herein, a hybrid strategy combining gas-atomization (involving in-situ reaction), CS, and post- friction stir processing was proposed to design a nano-TiB_2/AlSi10Mg composite. Multiscale characterization in terms of X-ray diffraction and scanning and transmission electron microscopy was conducted to track microstructure evolution for understanding the mechanisms determining mechanical performance of the as-produced composites. The results showed simultaneous improvement in both ultimate tensile strength (365 ± 35 MPa) and ductility (16.0 ± 1.2 %), which represents a breakthrough. The strengthening and toughing mechanisms were attributed to the fine matrix grains with the significantly improved metallurgical inter-particle bonding, and the uniformly distributed TiB_2 nanoparticles as reinforcement that was strongly bonded with the matrix (i.e. the formation of semi-coherent TiB_2/Al interface). This study provides new guidance for

hybrid additive manufacturing of metal matrix composites with high performance.

Keywords: Metal matrix composites; Cold spray; Additive manufacturing; Friction stir processing; Mechanical properties; Metallurgical bonding

1. Introduction

Cold spray (CS), as a solid-state deposition technique for surface coating, has recently been defined as an unconventional additive manufacturing (AM) process to fabricate net-shaped components and to repair damaged parts [1-3]. Unlike thermal spray and laser-based AM processes, CS uniquely relies on plastic deformation mechanisms of the highly accelerated micron-sized particles. Generally, the CS component is built layer-by-layer primarily through localized metallurgical bonding and mechanical interlocking, which corresponds to a relatively weak inter-particle (also called inter-splat) bonding [4-6]. Moreover, the localized work-hardening effect induced by the intensive plastic deformation of the particles significantly lowers its ductility, leading to a brittle feature of the CS deposit. Thus, very limited applications of CSAM have been exploited to structural load-bearing parts due to the unexpected premature failure.

So far, Al matrix composite (AMC) composites fabricated by CSAM have received increased attentions due to their high potentials for aircraft and marine applications. It has been widely accepted that certain mechanical properties (e.g. microhardness, wear performance) of the CS AMCs can be largely improved by properly integrating ceramic reinforcement particles into the Al matrix [7-11]. However, it is still challenging to obtain AMCs with high tensile performance owing to the poor bonding of the interfaces between Al matrix and ceramic particles and/or between inter-splats as well as some defaults (e.g. residual pores) within the composite deposits [12]. It was reported by Kumar et al. [13] that the CS SiC/Al composites were fractured at a very early stage with very low tensile strength and almost no ductility. The observation of fracture surface revealed a completely brittle feature with the fracture primarily occurred through poorly bonded interfaces of inter-splats and SiC/Al matrix.

Post-heat treatment (HT) and friction stir processing (FSP) are the most commonly used techniques to enhance mechanical properties of the CS components by improving the inter-particle bonding and reducing porosity and residual stress [1, 14, 15]. HT can partially heal the CS-induced defects through temperature-dependent atomic diffusion, while structure coarsening caused by high temperature often degrades the strength [15-17]. Furthermore, the interfacial bonding between metallic particle and ceramic particle can hardly be improved via atomic diffusion by HT, resulting in very limited improvement in tensile properties of the CS AMCs [18, 19]. Comparatively, severe plastic deformation involved in the FSP process can further modify the microstructure in the nugget zone, which not only produces fine and equiaxed grains but also increases the metallurgical inter-particle bonding [20] [21]. ***(should be [20,21])*** For instance, post-FSP has significantly increased the ultimate tensile strength (UTS) and elongation of CS pure Al by around 45% and 1336%, respectively [21]. Another advantage of post-FSP is to break down and then more homogenously redistribute the reinforcement particles in some AMCs. As a result, the strengthening effect of the second-phase particles is enhanced. For instance, it was found, in the CS SiC/5056Al composites, that the post-FSP resulted in the fine microstructure containing the redistributed and refined reinforcement particles, which was accompanied with improved hardness and wear performance [22-24].

However, to the authors' best knowledge, unlike the CS pure Al [21], the currently available results only showed limited improvement in strength-ductility trade-off for AMCs by the post-FSP. For example, post- FSP conditions were tentatively optimized to further improve tensile properties of the CS Al_2O_3/2024Al composite using mechanically mixed composite powder [18, 19]. However, the strength-ductility trade-off issue has not been solved mainly due to the presence of large Al_2O_3 particles and poor Al_2O_3/Al interfacial bonding induced by mechanical blending. Hence, it is considered that the selection of proper size and type of reinforcement in powder feedstock for CS is also critical in determining the final microstructure and properties tailored by FSP.

In the present work, a hybrid AM strategy combining gas-atomization (involving in-situ reaction), CS and post-FSP was proposed and validated and was used to design new AMCs with concurrently improved tensile strength and ductility. A specially designed Al matrix composite powder reinforced with in-situ formed TiB_2 particles was used as the feedstock to fabricate AMCs components by CSAM. By using such a specially designed composite powder, it is expected to solve the abovementioned major problems, like uneven distribution of reinforcements and poor interfacial bonding, involved in traditional CS process. Followed by CS, FSP treatment was applied to modify the microstructure, reduce the defects, and improve the mechanical property of the CS TiB_2/AlSi10Mg composites. Balanced UTS (365 MPa) and ductility (elongation of 16.0 %) were simultaneously achieved in the final composite. The strengthening mechanisms of the AMCs related to the microstructure evolution were discussed in detail.

2. Experimental details

2.1 CS deposition and FSP treatment

A specially designed 7.0 wt. % TiB_2/AlSi10Mg composite powder was produced by in-situ chemical reaction using the mixed K_2TiF_6 and KBF_4 salts in molten Al followed by gas atomization. Details about the processing parameters and conditions were reported elsewhere [25, 26]. The chemical composition of the powder is 9.81 wt.% Si, 0.32 wt.% Mg, 7.0 wt.% TiB_2 (~4.3 vol.%) with Al balance, measured through inductively coupled plasma atomic emission analysis (ICP-AES). The composite powder as well as the pure AlSi10Mg powder after sieving were used as the feedstocks for CS.

A homemade helium circulation CS system (LERMPS, UTBM, France) was used to build a component with over 2.5 mm thick onto grit-blasted Al substrates (140×80×4 mm). Helium was used as the propellant and carrier gases with an inlet pressure and temperature of 1.8 MPa and 320 °C, respectively. Nozzle standoff distance and traverse

speed were set to 30 mm and 100 mm/s, respectively. Post-FSP was done using a commercial friction stir welding machine (FSW-RL31-010, Beijing FSW Technology Co., Ltd, China), equipped with an H13 steel stir-tool with a threaded pin of 3.5 mm in root diameter and 2.0 mm in length, and a concave shoulder of 10 mm in diameter. Rotation and traverse speeds were set to 1500 rpm and 500 mm/min, respectively. The tool was set to a 2.5° tilt angle to avoid surface defects. The as-acquired samples are shown in **Fig. 1a**. The same CS and FSP processes were applied to the gas-atomized AlSi10Mg powder (without TiB_2 particles) for comparison.

2.2 Materials characterization

The as-sprayed deposits before and after FSP treatment as well as powders were examined by an X-ray diffractometer (Siemens D5000, Germany) with the Co (λ =1.78897 Å) source at a current of 40 mA, a voltage of 35 kV and scan step of 0.02°.

Polished cross-sectional microstructures of the samples were observed using an optical microscope (Nikon, Japan) and a scanning electron microscope (SEM) equipped with an energy-dispersive spectroscopy unit (JSM5800LV, JEOL, Japan). Average porosities of samples were determined by analyzing five cross-sectional images using ImageJ software (ImageJ, NIH, Bethesda, Md.). To clearly observe the microstructure, specimens were polished and etched at room temperature using Kroll's reagent (3ml HF + 6ml HNO_3 + 100ml H_2O). Another SEM instrument (JSM7800F, JEOL, Japan) equipped with an EBSD detector from Oxford instruments was employed to reveal information about grain structure. Samples for SEM/EBSD characterization were prepared by mechanical polishing and final surface iron milling using a Fischione instruments model 1060 miller. EBSD measurements were conducted on the cross-sections of deposits at an electron energy of 25 KeV and with a step size of 100 nm. An FEI Tecnai G2 microscope, operating at 200 kV, was used for transmission electron microscopy (TEM) characterization. Cross-sectional TEM samples were prepared by mechanical polishing followed by final ion milling using a Gatan Model 691 precision ion polishing system.

Microhardness measurements were performed on the cross-section of the deposits using a Vickers hardness indenter (Leitz, Germany) with a load of 100g for 15s. Ten measurements for each sample were conducted to have an average value. A medium-sized tensile specimen, with the width in the gauge section of 2 mm, total length of 37 mm and thickness of 2 mm, was tested using a Zwick/Roell Z100 machine at a strain rate of 1 mm/min. The location and the dog-bone specimen size are shown in **Fig. 1b**.

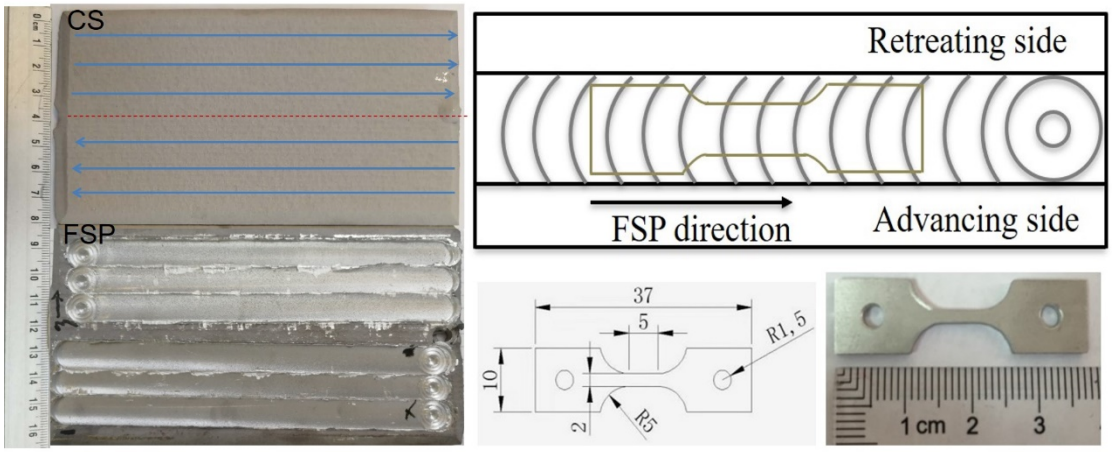

Fig. 1 (a) Photograph of the as-sprayed TiB_2/AlSi10Mg composite parts before and after FSP treatment. (b) Schematic diagram of FSP and dimension size of the samples used for tensile testing.

3. Results

3.1 Composite powder characterization

As shown in **Fig. 2a**, the gas-atomized composite powder exhibits a near-spherical shape having an average particle size of 37 μm (see **Fig. 2c**). Apart from a few residual particle clusters as marked by red circles in **Fig. 2b**, the fine TiB_2 reinforcement particles are homogeneously distributed within the composite particle. A close look (**Fig. 2d**) reveals that the TiB_2 nanoparticles tend to be segregated at the α-Al grain boundaries along with the well-connected network of eutectic Si particles (**Fig**. **2b** and **d**). The equiaxed Al grains in the matrix are in the size ranging from 1 to 5 μm with an average of around 2.6 μm (**Fig. 2e** and **f).**

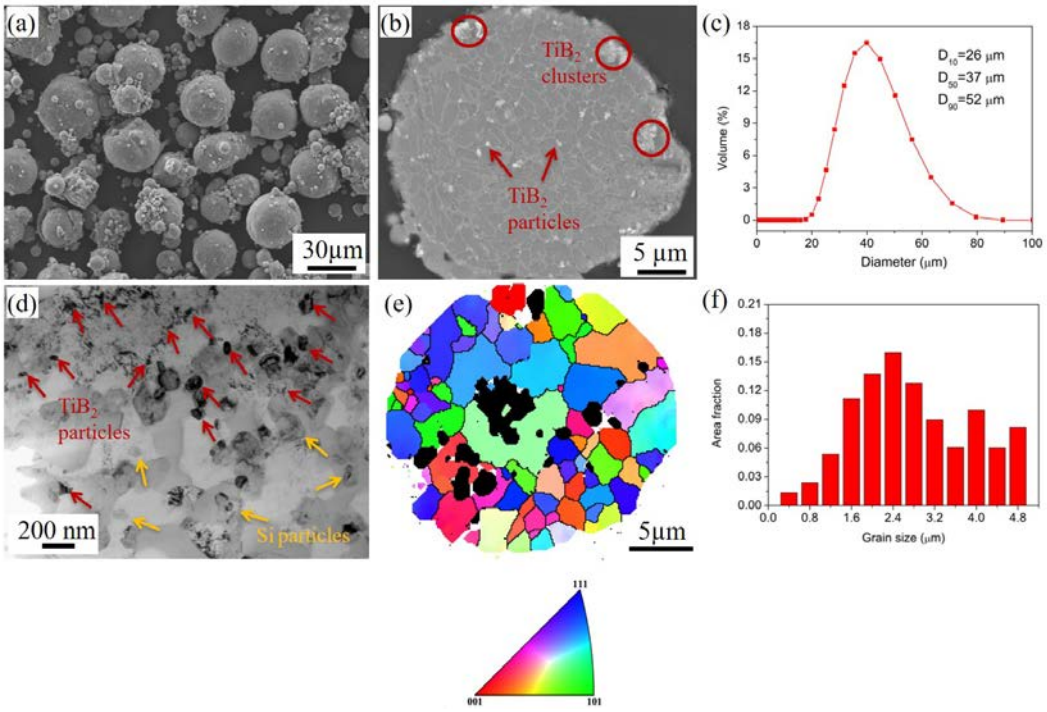

Fig. 2 Microstructure of the gas-atomized TiB_2/AlSi10Mg composite powder: SEM images showing (a) particles and (b) cross-sectional morphology of a typical particle; (c) particle size distribution measured by laser diffraction; (d) TEM bright-field (BF) image showing the distributions of TiB_2 nanoparticles (marked by red arrow) and Si particles (marked by yellow allow); (e) cross-sectional SEM/EBSD orientation map of the composite particle (dark contrasts are indexed as TiB_2 particle clusters) and (d) corresponding size distribution of Al grains.

3.2 Phase composition

Fig. 3a and **b** display the XRD patterns of the pure AlSi10Mg and TiB_2/AlSi10Mg composite powders, deposits before and after FSP treatment. The composition phases, including α-Al, Si, and Mg_2Si, in the as-sprayed AlSi10Mg powder, were well preserved in the CS and FSP treated samples. In addition to these three phases, peaks corresponding to the TiB_2 phase can be observed on the composite patterns. Moreover, XRD patterns of the pure AlSi10Mg and TiB_2/AlSi10Mg composite samples show that Si peaks of FSP treated samples have higher intensities than those in the as-sprayed state. This indicates a significant decrease of Si solid solubility in Al caused by the thermal effect during FSP, as the temperature in the stir zone can be of the order of 80 %

of the melting temperature of the Al alloys [27].

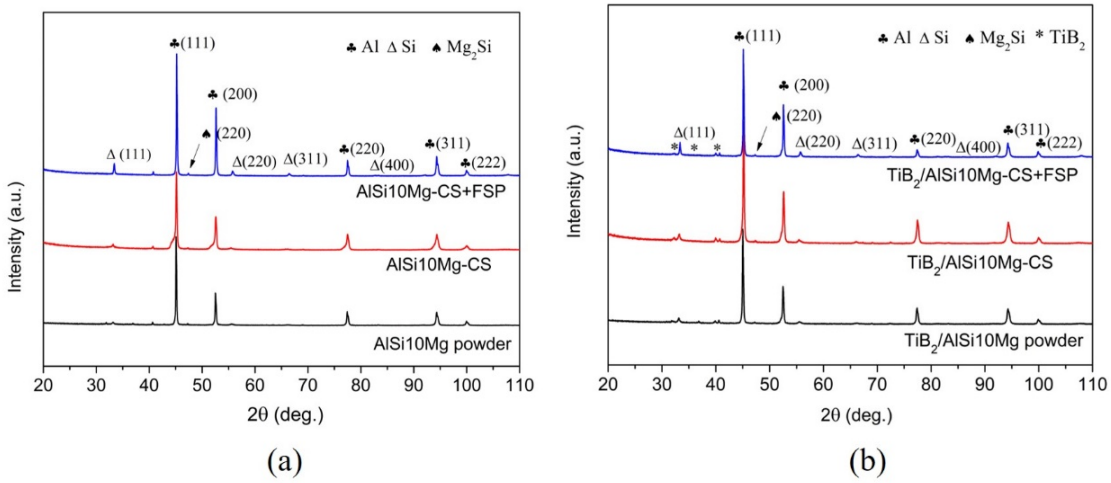

Fig. 3 XRD patterns of the CS and FSP treated deposits: (a) AlSi10Mg; (b) TiB_2/AlSi10Mg composite.

3.3 Microstructure evolution

Fig. 4a and **b** show the microstructure with visibly deformed splat morphology of the CS pure AlSi10Mg and TiB_2/AlSi10Mg composite deposits, respectively. The evidence of inter-splat boundaries as well as some small pores located in the junction areas clearly indicate the weak metallurgical inter-particle bonding due to insufficient plastic deformation, the fundamental weakness of CS even though helium was used as the propellant gas. The porosity measurements yield around 0.35% and 0.24% for the pure AlSi10Mg and TiB_2/AlSi10Mg composite deposits, respectively. The magnified images in **Fig. 5a** and **b** demonstrate the eutectic Si particles around α-Al grains, which are well preserved from the initial powders. In addition to the eutectic Si particles, finer dispersed Si nanoparticles precipitated from the supersaturated Al matrix are also presented due to the thermal softening effect during CS. The clusters and uneven distribution of the TiB_2 nanoparticles in the initial powder are retained in the CS composite component (**Fig. 4b and Fig. 5b**). The TEM image in **Fig. 8a** ***(description of Fig. 8 is before figures 6 and 7 ???)*** confirms that TiB_2 clusters and nanoparticles are primarily dispersed at grain boundaries, while the Si nanoparticles are located not only at grain boundaries but also inside the α-Al cells.

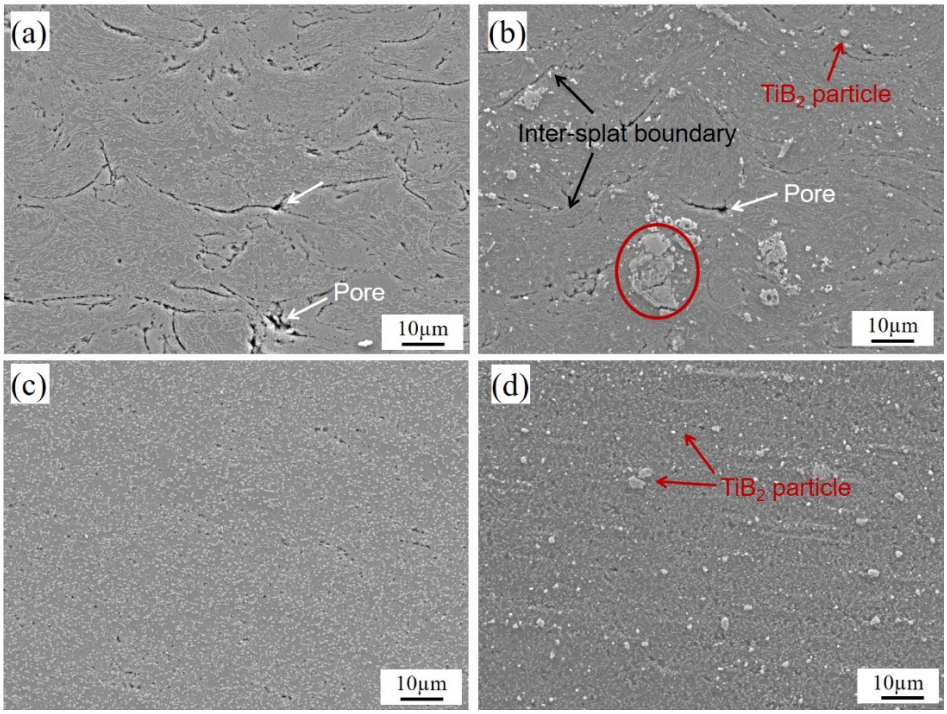

Fig. 4 SEM images showing the cross-sectional morphologies of the (a, b) CS and (c, d) CS+FSP samples in low magnification: (a) and (c) AlSi10Mg; (b) and (d) TiB_2/AlSi10Mg composite.

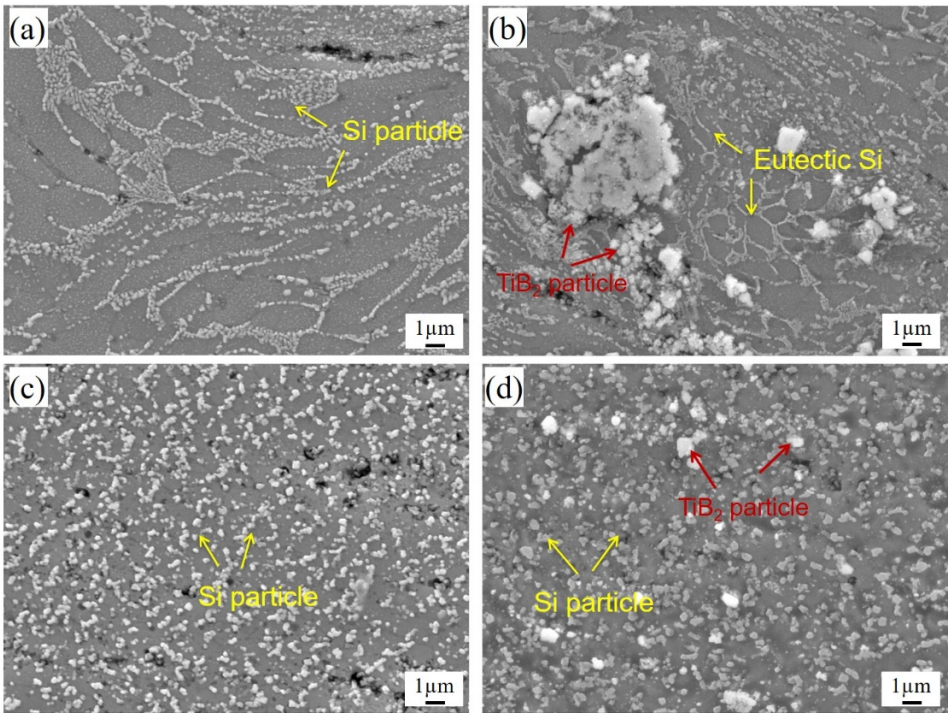

Fig. 5 SEM images showing the cross-sectional morphologies of the (a, b) CS and (c, d) CS+FSP samples in high magnification: (a) and (c) AlSi10Mg; (b) and (d) TiB_2/AlSi10Mg composite.

Based on the EBSD orientation maps (**Fig. 6a and b)**, both the CS pure AlSi10Mg and TiB_2/AlSi10Mg composite samples display bimodal grain size distributions containing a large number of ultrafine gains at the inter-particle boundaries and deformed micron-sized grains within the particles (see **Fig. 7a and b**). Formation of these ultrafine grains can be attributed to the dynamic recrystallization via dislocation accumulation and sub-grain rotation at a high strain-rate during high-velocity particle impact [28-30]. Nevertheless, both the CS pure AlSi10Mg sample and TiB_2/AlSi10Mg composite sample have average grain sizes of about 1.5 μm.

Comparatively, **Fig. 4c** and **d** show that the FSP treated samples in the nugget zone are fully dense without visible pores (porosity less than 0.2%) and inter-splat boundaries, indicating the enhanced metallurgical bonding. Eutectic Si structure in the as-sprayed state disappeared and presented as nanosized Si individual particles after FSP treatment. According to EBSD maps shown in **Fig. 6c** and **d**, both the deposits display a homogenous structure containing equiaxed fine grains. A homogeneous structure is commonly observed in the FSP treated samples, which can be explained by the continuous dynamic recrystallization, in which a continuous introduction of strain is coupled with rapid recovery and the migration of sub-grain/boundaries [31, 32]. During FSP, the material in the stir zone experienced severe deformation, which continuously induced a very high density of dislocations. With the continued deformation, the stored energy contained in these dislocations drove the dynamic recovery and recrystallisation processes. The composite sample has an average size of about 1.4 μm, which is slightly smaller than that of the pure AlSi10Mg sample (~1.6 μm). The more refined grains of the composite sample may be due to the presence of TiB_2 nanoparticles, which can prevent the migration of dislocations and recovery process.

As shown in **Fig. 4d** and **Fig. 5d**, the TiB_2 clusters presented in the CS state were broken into fragments, resulting in more homogenous particle distribution. Close observation by TEM shows that the majority of TiB_2 and precipitated Si nanoparticles are redistributed homogenously inside the Al grains (**Fig. 8b**). The well-defined ring

patterns in Fig. 8c confirm the formation of Si nanoparticles in the ultrafine Al grain matrix. However, it is difficult to identify the TiB_2 and possible Mg_2Si particles due to their low quantity only contributing to satellite spots in the SAED pattern. The TEM image in **Fig. 9a** highlights that the TiB_2 nanoparticles are tightly bonded with the Al matrix, showing one of the principal orientation relationships (ORs): $[2\bar{1}\bar{1}0]_{TiB_2}$ // $[101]_{Al}$ and $(0001)_{TiB_2}//(\bar{1}11)_{Al}$ (**Fig. 9b** and **c**). This OR is consistent with previous literature [33, 34]. The overall semi-coherent TiB_2/Al interface due to the in-situ chemical reaction in the melt contributed to the formation of the high interfacial bonding [34].

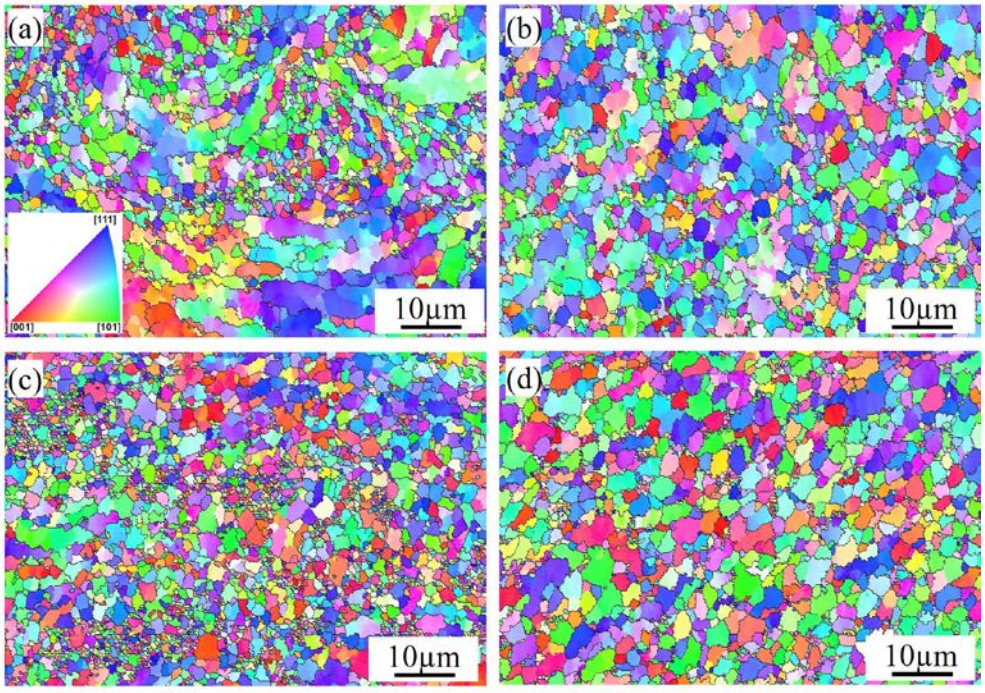

Fig. 6 SEM/EBSD orientation maps of the (a, b) CS and (c, d) CS+FSP samples in high magnification: (a) and (c) AlSi10Mg; (b) and (d) TiB_2/AlSi10Mg composite.

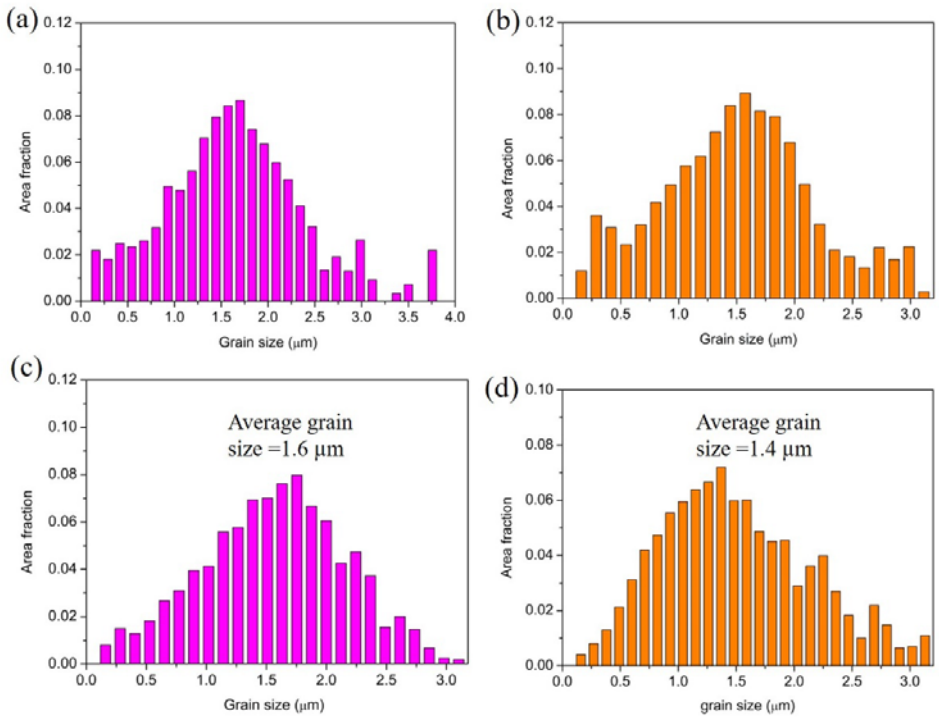

Fig. 7 Grain size distributions of the (a, b) CS and (c, d) CS+FSP samples according to EBSD analysis: (a) and (c) AlSi10Mg; (b) and (d) TiB_2/AlSi10Mg composite.

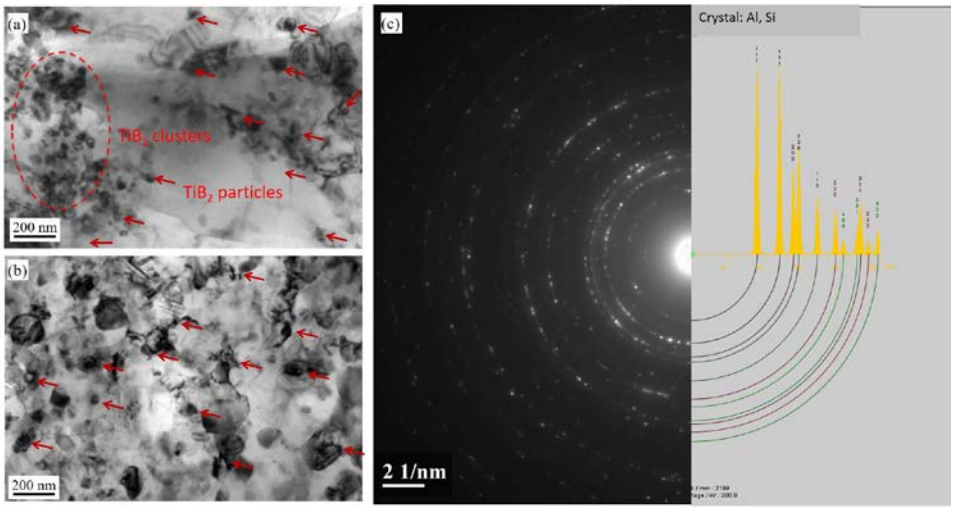

Fig. 8 TEM BF images showing the TiB_2 particle distributions of the TiB_2/AlSi10Mg composite deposits (a) before and (b) after FSP treatment. (c) selected area electron diffraction (SAED) pattern of the post FSP sample where only Al and Si phases can be determined without ambiguity from the overlapped ring patterns

(Comments of Fig. 8C: (hkl) miller indices are too small to be visible, you should manually add them. Also use different colors to distinguish Si and Al)

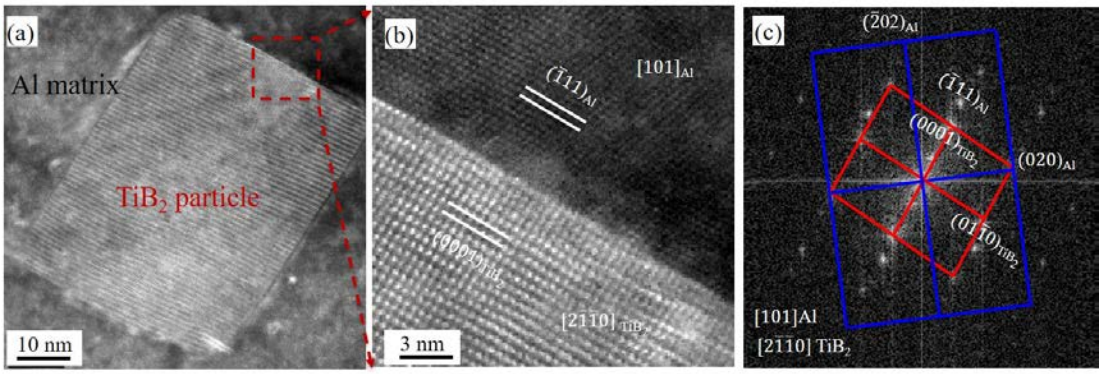

Fig. 9 (a) TEM image showing a faceted TiB_2 particle in the Al matrix, (b) high-resolution TEM image highlighting the TiB_2/Al interface in the box area in (a), and (c) corresponding fast Fourier transform (FFT) pattern of (b).

3.4 Mechanical properties

3.4.1 Microhardness

Fig. 10 illustrates the microhardness values measured on the cross-section of the CS and CS+FSP treated samples. The microhardness of the as-sprayed AlSi10Mg deposit is about 139±4$HV_{0.1,}$ which is two times that of the as-casted (67 $HV_{0.1}$) [35]. This significant increment in microhardness can be explained by the enhanced work hardening effect as a result of severe plastic deformation of the particles during CS deposition. Since He was used in this study to accelerate the particles to a very high velocity, the particles would be largely deformed and lead to a large amount of residual stress and dislocations within the matrix, which contribute significantly to increase the microhardness in the as-sprayed state. The as-sprayed composite deposit reaches a higher value of 179±5 $HV_{0.1}$, showing about 22% increment compared to that of the pure AlSi10Mg deposit. The increased microhardness in composite deposit should be attributed to the uniformly distributed TiB_2 particles in the Al matrix.

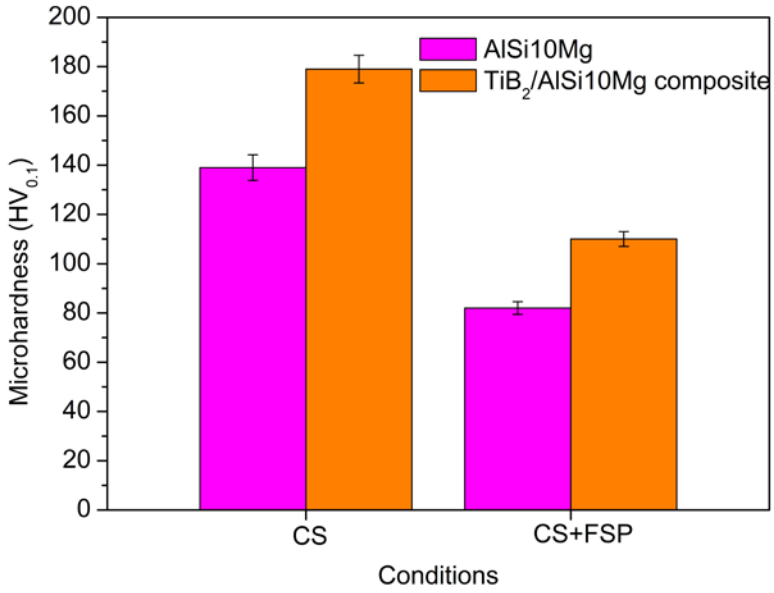

Fig. 10 Microhardness values of the CS and CS+FSP treated samples.

The microhardness of the composite deposits in the stir zone is about 110±3 $HV_{0.1}$, which is much higher than that of the pure AlSi10Mg sample (82 $HV_{0.1}$) due to the reinforcement of nano/micro TiB_2 particles. Nevertheless, the microhardness of the FSP treated samples show a significant decrement compared to the as-sprayed states. Since the grain size changed a little after FSP treatment, residual stress relaxation induced by the thermal softening effect and recovery process should be mainly responsible for the decreased microhardness.

3.4.2 Tensile properties

As shown in **Fig. 11a**, CS samples (the AlSi10Mg alloy and the TiB_2/AlSi10Mg composite) prematurely failed (elongation < 1.0%) due to the poor inter-splat bonding and enhanced work hardening effect, which is commonly observed in most CS samples [17, 36]. The post-FSP led to a dramatic improvement in UTS and elongation of both materials to 295 ± 30 MPa and 21 ± 0.8 % for the AlSi10Mg alloy, and 365 ± 35 MPa and 16 ± 1.2 % for the TiB_2/AlSi10Mg composite. The composite also exhibited a slightly higher work hardening capacity than the AlSi10Mg sample during plastic deformation before yielding point (**Fig. 11b**). Compared with many other CS and post-treated AMCs reported in the literatures displaying the strength-ductility trade-off, the

present result shows an outstanding balance of strength and ductility, representing a breakthrough for this type of composite materials as shown in **Fig. 11c**.

The typical fracture surfaces of both CS samples show primary brittle fracture along with inter-splat interfaces and the intergranular fracture (as exemplified in **Fig. 12a** and **d**), while those of both post-FSP samples show the highly ductile rupture mode dominated by fine dimples (**Fig. 12b** and **c**). The dimple size (a few microns) is related to the grain size as Grain boundaries act as sites for crack nucleation to control the size of the dimples. The dimple size of the composite is slightly smaller than that of the AlSi10Mg alloy, agreeing with the statistical distributions of grain size (**Fig. 7c** and **d**). The dispersed TiB_2 and Si nanoparticles refined the recrystallized grains by promoting grain nucleation and hindering grain coarsening, while the additional effect of TiB_2 nanoparticle is limited in the composite. The fact that the nanoparticles are visible at bottoms of the dimples suggests the ductile rupture by decohesion of the Si/Al and/or TiB_2/Al interfaces.

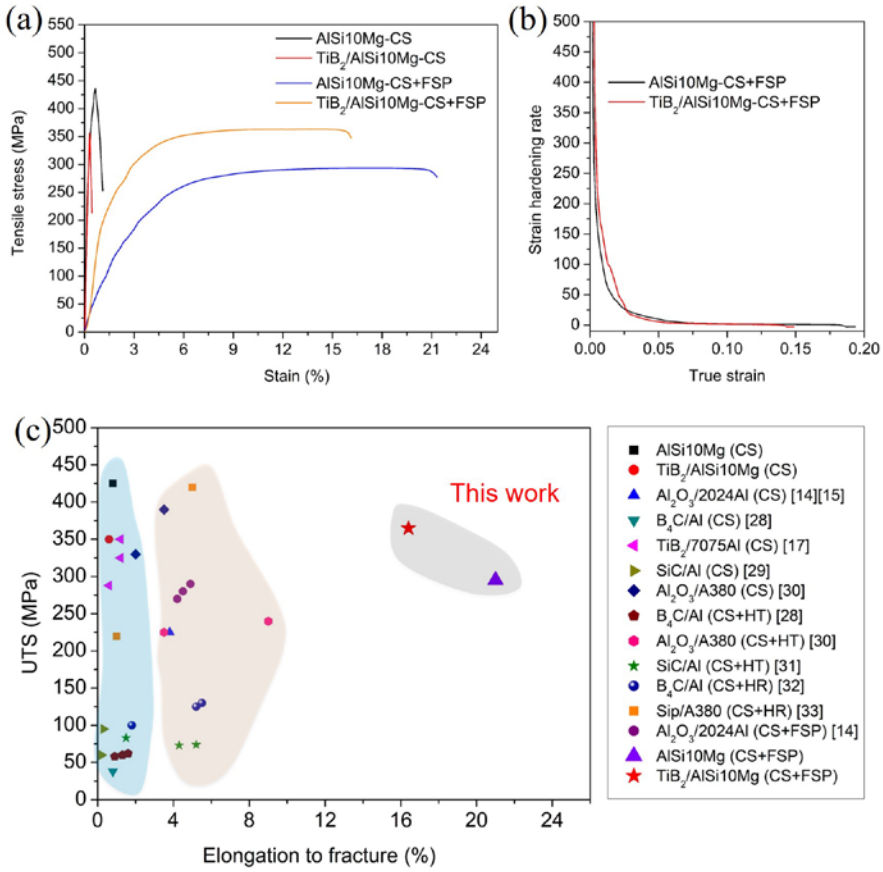

Fig. 11 (a) Tensile stress-strain curves for the AlSi10Mg alloy and the TiB_2/AlSi10Mg composite at CS and after post-FSP. (b) Strain hardening rate as a function of true strain obtained from the tensile -strain curves. (c) Comparison of the ultimate tensile strength and elongation values of our samples with other AMCs processed by CS, CS + HT, CS + hot rolling (HR), and CS+FSP treatments [12, 13, 18, 19, 26, 37-40].

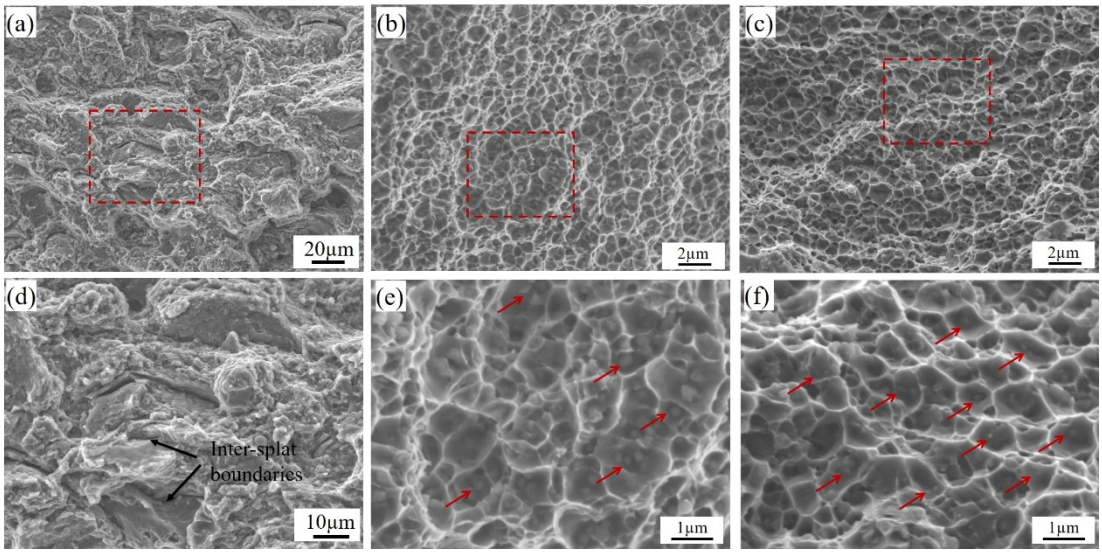

Fig. 12 SEM images showing the fracture surfaces of the CS TiB_2/AlSi10Mg composite

(a, d) and post-FSP AlSi10Mg alloy (b, e) and post-FSP TiB_2/AlSi10Mg composite (c, f); (d-f) are the corresponding magnified images in the box regions in (a-c). The red arrows in (e) and (f) indicate the nanoparticles located at the bottoms of dimples. Note that the CS AlSi10Mg sample shows a similar fracture surface.

4. Discussions

4.1 Insight into the key factors determining mechanical performance of CS AMCs

For a certain MMC, it is well established that the final mechanical properties depend largely on the following four factors [25, 41, 42]: i) interior defect level; ii) matrix texture and grain size; ii) reinforcement particle size and distribution; and iv) interfacial bonding state between the reinforcement particle and the matrix. Here, as illustrated in **Fig. 13,** we are trying to establish the relationship between these factors and mechanical properties of CS AMCs prepared by different methods**.**

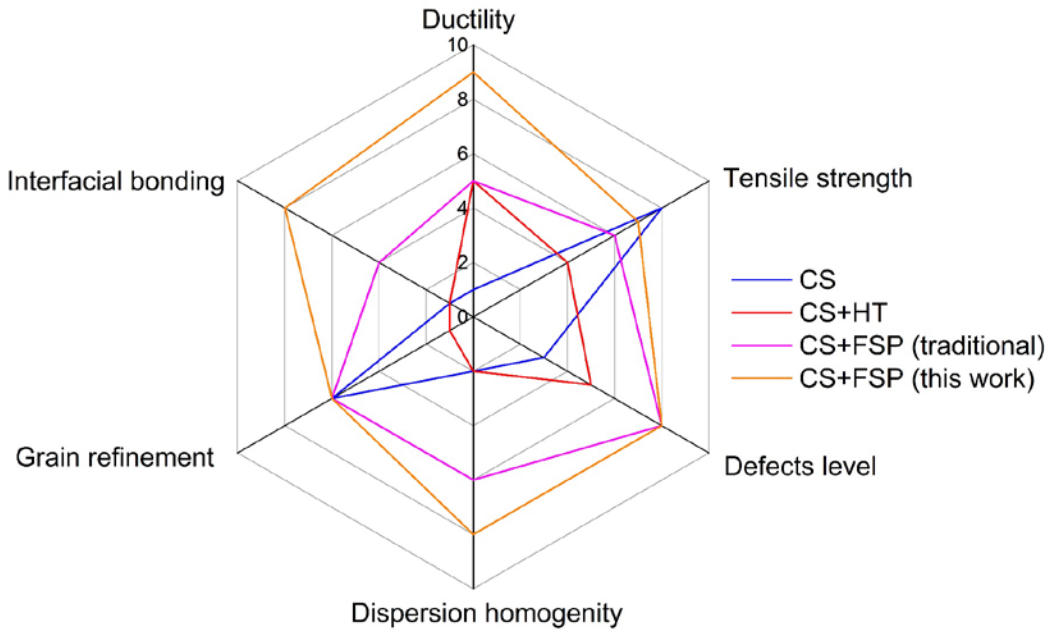

Fig. 13 Radar chart of defect level, reinforcement dispersion homogeneity, grain refinement, and interfacial bonding versus mechanical properties of CS AMCs prepared

by different methods.

Importantly, free of any processing defects is the starting point before the correlation between microstructure (e.g. grain structure and TiB_2 particles) and properties can be properly done. Generally, a higher particle impact velocity leads to enhanced plastic deformation and metallic bonding of the deformed splats in CS process. However, there are still some interior defects, such as pores and poor inter-splat boundaries, presented in the as-sprayed state even though helium was used as the propellent gas. Considering that a fracture could primarily take place around these defects, it is vitally important to obtain a fully dense and defect-free structure. HT can partially heal micro-pores and tightly bonded inter-splat interfaces though atomic diffusion. It should be emphasized that the post-FSP treatment effectively altered the prominent mechanical interlocking in the CS state to the full metallurgical inter-splat bonding. Significant improvement of tensile properties, particularly the ductility, of both the AlSi10Mg alloy and the TiB_2/AlSi10Mg composite after post-FSP (**Fig. 11**) witnesses the elimination of such defects, introduced by CS. Accordingly, it promoted the transition from the brittle to ductile fracture mode in the post-FSP samples (**Fig. 12**), whatever the TiB_2 reinforcement particles get involved or not.

The microstructure of the initial composite powder can be well preserved in the CS deposit except that high strain stress and numbers of fine grains were generated near highly deformed inter-splat boundaries. These ultrafine grains and the localized work hardening effect could increase the microhardness and strength of the CS deposit, but remarkably reduce the ductility. During FSP, the material in the SZ ***(did you define SZ before?)*** experienced severe deformation, which continuously drove the dynamic recovery and recrystallisation processes. Compared to the as-sprayed state, a homogenous structure with fine grains (0.5-3 μm) and more uniformly distributed residual stress were obtained for both the pure AlSi10Mg and TiB_2/AlSi10Mg composite samples after FSP treatment (**Fig. 6 c** and **d**). More importantly, the vigorous stirring action of the rotating tool fractured the clusters (agglomerated TiB_2 nanoparticles) into homogeneously distributed individual TiB_2 nanoparticles in Al

matrix [43]. It should be highlighted that post-FSP treatments of CS AMCs in the previous studies failed to fracture the micron-scaled reinforcement particles into nanoscales using the mechanical blended mixtures [18, 19].

As revealed by TEM images (**Fig. 9**), the robust interfacial bonding between the reinforcement particle and Al matrix was successfully induced by using the gas atomized in-situ TiB_2/AlSi10Mg composite powder. Such a semi-coherent interface cannot be achieved by CS of mechanical blended powders even after FSP treatment. That is to say the initial state of the composite powder is of great necessary to achieve the designed mechanical performance. Therefore, the abovementioned four critical issues for producing AMCs were successfully overcome by CS of gas-atomized composite powder followed by post-FSP.

4.2 Possible strengthening and toughening mechanisms

To understand the strengthening behavior of TiB_2 nanoparticles in the composites, several aspects should be considered, e.g. the dispersion of TiB_2 nanoparticles, grain refinement induced by TiB_2 particles, load transfer between TiB_2 nanoparticles and Al matrix. The homogenous fine-grained structure decorated by the uniformly distributed TiB_2 nanoparticles is highly beneficial for the enhancement of both tensile strength and ductility. This is because the TiB_2 clusters formed in the initial powder (**Fig. 1)** and almost remained in the CS component (**Fig. 4**) can result in stress concentration that significantly degrades ductility. The TiB_2 nanoparticles homogeneously redistributed inside the micron-sized grains in the matrix at the post-FSP state increased the effectiveness of the Orowan strengthening ($\Delta\sigma_{Orowan}$). The contribution from the dispersed TiB_2 nanoparticles is estimated by the following equation [44]:

$$\Delta\sigma_{Orowan} \approx \Delta\sigma_{Orowan,TiB_2} = \frac{0.13G_m b}{\lambda}\ln\left(\frac{d_{p,TiB_2}}{2b}\right) \quad (1)$$

$$\lambda = d_{p,TiB_2}\left[\left(\frac{1}{2V_{p,TiB_2}}\right)^{1/3} - 1\right] \quad (2)$$

Where G_m and b are the shear modulus of the matrix (~26.5 GPa) and the Burgers vector (~0.286 nm) [25] [45], respectively. V_{p,TiB_2} and d_{p,TiB_2} are the volume fraction (~3.6 vol.%) and the average size of the TiB_2 (~100 nm), respectively. λ is the inter-particle spacing. As such, the calculated $\Delta\sigma_{Orowan}$ is 36.3 MPa.

The contribution by grain refinement (Hall-Petch equation) can be expressed as follows [46]:

$$\Delta\sigma_{\text{Hall-Petch}} = k\left[d^{-\frac{1}{2}} - d_0^{-\frac{1}{2}}\right] \quad (3)$$

where k is a constant (~50 MPa/√(μm)) [46], d and d_0 are the average grain size of the composite and unreinforced AlSi10Mg sample, respectively. Using the average grain sizes obtained from the SEM/EBSD analyses (**Fig. 7c** and **d**), the strengthening effect due to further grain refinement is estimated to be only 2.73 MPa in the composite sample.

Moreover, our TEM results (**Fig. 9b** and **c**) show the OR between the TiB_2 nanoparticle and Al matrix, suggesting the strong TiB_2/Al interfacial bonding, which ensures an effective load transfer from matrix to nanoparticles [25, 43]. The load-bearing mechanism is in this case responsible for the improved tensile strength of the composite. It can be described as below [47]:

$$\Delta\sigma_{load} = 1.5V_{p,TiB_2}\sigma_i \quad (4)$$

According to the previous study [25], the bonding strength between the nano-particles and the Al-Si matrix σ_i can be estimated to be around 676 MPa. Thus, the contribution due to the load-bearing mechanism leads to an increment in the strength of around 36.5 MPa in the composite sample. Compared with the post-FSP AlSi10Mg sample, the total increment of tensile strength is around 70 MPa in the post-FSP composite (**Fig. 11a**). This was attributed to the Orowan strengthening and load-bearing mechanisms promoted by the dispersed TiB_2 nanoparticles.

The enhanced ductility in the post-FSP composite sample may be explained as

follows: i) the presence of a large number of Grain boundaries in the fine-grained matrix (0.5-3 μm) contributed to the enhancement of plastic flow and ductility by providing a tortuous path for the crack propagation during yielding and necking processes [48]. ii) Both the dispersed TiB_2 and Si nanoparticles promote dislocation plasticity and storage during deformation increasing the work hardening rate of the composite (**Fig. 11b**). The increased work hardening rate offers a uniform deformation capability equivalent to that of the matrix, thereby enhancing the ductility of the composite [25, 44]. iii) The presence of an OR between intragranular TiB_2 nanoparticles and the Al matrix (**Fig. 9c**) may also help diminish stress localization and early fracture [44]. Therefore, introducing the uniform dispersion of TiB_2 nanoparticles in the grain interior is an effective approach to increase the strength and simultaneously improve the ductility of the composites, because they can generate, pin down, and thus accumulate dislocations within the grains [49-51].

5. Conclusions

In this study, a novel gas-atomized composite powder reinforced with in-situ TiB_2 particles was used as the feedstock to fabricate TiB_2/AlSi10Mg composite using CS followed by post-FSP treatment. The following conclusions can be drawn:

(1) The CS TiB_2/AlSi10Mg composite deposits displayed a dense structure with some TiB_2 clusters distributed in the Al matrix.

(2) Both the as-sprayed pure AlSi10Mg and TiB_2/AlSi10Mg composite deposits possessed high tensile strength but almost no ductility due to the limited metallurgical bonding and work hardening effect.

(3) FSP treatment altered the inter-splat bonding conditions from interlocking or partially metallurgical bonding in the as-sprayed state to a fully metallurgical bonding state.

(4) Simultaneous enhancement in tensile strength and ductility of the CS TiB_2/AlSi10Mg composite has been achieved by FSP treatment via redistributing and refining of TiB_2 nanoparticles and enhancing interfacial bonding due to the in-

situ chemical reaction during gas atomization.

Acknowledgments

Financial support of X.L. XIE's Ph.D. thesis was from the China Scholarship Council (No. 201604490100), Université Bourgogne - Franche-Comté, and Centre National de la Recherche Scientifique (CNRS). The microscopy facilities in Lille (France) are supported by the Conseil Régional du Nord-Pas de Calais, and the European Regional Development Fund (ERDF). G. JI thanks Campus France for providing travel funding through the PHC Xu Guangqi program (No. 45597XK). Prof. M.X. ZHANG (University of Queensland, Australia) was thanked for paper revision.

References

[1] Shuo Yin, Pasquale Cavaliere, Barry Aldwell, Richard Jenkins, Hanlin Liao, Wenya Li, Rocco Lupoi, Cold spray additive manufacturing and repair: Fundamentals and applications, Addit. Manuf., 21 (2018), 628-650.

[2] Wenya Li, Kang Yang, Shuo Yin, Xiawei Yang, Yaxin Xu, Rocco Lupoi, Solid-state additive manufacturing and repairing by cold spraying: A review, J. Mater. Sci. Technol., 34 (2018), 440-457.

[3] Shuo Yin, Yingchun Xie, Jan Cizek, Emmanuel J Ekoi, Tanvir Hussain, Denis P Dowling, Rocco Lupoi, Advanced diamond-reinforced metal matrix composites via cold spray: properties and deposition mechanism, Composites Part B, 113 (2017), 44-54.

[4] Yingchun Xie, Shuo Yin, Chaoyue Chen, Marie-Pierre Planche, Hanlin Liao, Rocco Lupoi, New insights into the coating/substrate interfacial bonding mechanism in cold spray, Scripta Mater., 125 (2016), 1-4.

[5] Shuo Yin, Xiaofang Wang, Xinkun Suo, Hanlin Liao, Zhiwei Guo, Wenya Li, Christian Coddet, Deposition behavior of thermally softened copper particles in cold spraying, Acta Mater., 61 (2013), 5105-5118.

[6] C Borchers, F Gärtner, T Stoltenhoff, H Kreye, Microstructural bonding features of cold sprayed face centered cubic metals, J. Appl. Phys., 96 (2004), 4288-4292.

[7] Onur Meydanoglu, Bertrand Jodoin, E Sabri Kayali, Microstructure, mechanical properties and corrosion performance of 7075 Al matrix ceramic particle reinforced

composite coatings produced by the cold gas dynamic spraying process, Surf. Coat. Technol., 235 (2013), 108-116.
[8] M Yu, XK Suo, WY Li, YY Wang, HL Liao, Microstructure, mechanical property and wear performance of cold sprayed Al5056/SiCp composite coatings: effect of reinforcement content, Appl. Surf. Sci., 289 (2014), 188-196.
[9] Xiang Qiu, Ji-qiang Wang, Jun-rong Tang, Lawrence Gyansah, Zhi-po Zhao, Tian-ying Xiong, Microstructure, microhardness and tribological behavior of Al2O3 reinforced A380 aluminum alloy composite coatings prepared by cold spray technique, Surf. Coat. Technol., 350 (2018), 391-400.
[10] Xiawei Yang, Wenya Li, Siqi Yu, Yaxin Xu, Kaiwei Hu, Yaobang Zhao, Electrochemical characterization and microstructure of cold sprayed AA5083/Al2O3 composite coatings, J. Mater. Sci. Technol., (2020),
[11] Wenya Li, Hamid Assadi, Frank Gaertner, Shuo Yin, A review of advanced composite and nanostructured coatings by solid-state cold spraying process, Critical Reviews in Solid State and Materials Sciences, 44 (2019), 109-156.
[12] NH Tariq, L Gyansah, JQ Wang, X Qiu, B Feng, MT Siddique, TY Xiong, Cold spray additive manufacturing: A viable strategy to fabricate thick B4C/Al composite coatings for neutron shielding applications, Surf. Coat. Technol., 339 (2018), 224-236.
[13] S Kumar, Sai Kiran Reddy, Shrikant V Joshi, Microstructure and performance of cold sprayed Al-SiC composite coatings with high fraction of particulates, Surf. Coat. Technol., 318 (2017), 62-71.
[14] Shuo Yin, Jan Cizek, Xingchen Yan, Rocco Lupoi, Annealing strategies for enhancing mechanical properties of additively manufactured 316L stainless steel deposited by cold spray, Surf. Coat. Technol., (2019),
[15] Pierre Coddet, Christophe Verdy, Christian Coddet, François Debray, On the mechanical and electrical properties of copper-silver and copper-silver-zirconium alloys deposits manufactured by cold spray, Mater. Sci. Eng., A, 662 (2016), 72-79.
[16] Renzhong Huang, Michiyoshi Sone, Wenhua Ma, Hirotaka Fukanuma, The effects of heat treatment on the mechanical properties of cold-sprayed coatings, Surf. Coat. Technol., 261 (2015), 278-288.
[17] Shuo Yin, Richard Jenkins, Xingchen Yan, Rocco Lupoi, Microstructure and mechanical anisotropy of additively manufactured cold spray copper deposits, Mater. Sci. Eng., A, 734 (2018), 67-76.
[18] Kang Yang, Wenya Li, Chunjie Huang, Xiawei Yang, Yaxin Xu, Optimization of

cold-sprayed AA2024/Al2O3 metal matrix composites via friction stir processing: Effect of rotation speeds, J. Mater. Sci. Technol., 34 (2018), 2167-2177.
[19] Kang Yang, Wenya Li, Pengliang Niu, Xiawei Yang, Yaxin Xu, Cold sprayed AA2024/Al2O3 metal matrix composites improved by friction stir processing: Microstructure characterization, mechanical performance and strengthening mechanisms, J. Alloys Compd., 736 (2018), 115-123.
[20] Chunjie Huang, Wenya Li, Yan Feng, Yingchun Xie, Marie-Pierre Planche, Hanlin Liao, Ghislain Montavon, Microstructural evolution and mechanical properties enhancement of a cold-sprayed CuZn alloy coating with friction stir processing, Mater. Charact., 125 (2017), 76-82.
[21] Wen Wang, Peng Han, Yinghui Wang, Ting Zhang, Pai Peng, Ke Qiao, Zhi Wang, Zhihao Liu, Kuaishe Wang, High-performance bulk pure Al prepared through cold spray-friction stir processing composite additive manufacturing, Journal of Materials Research and Technology, 9 (2020), 9073-9079.
[22] KJ Hodder, H Izadi, AG McDonald, AP Gerlich, Fabrication of aluminum–alumina metal matrix composites via cold gas dynamic spraying at low pressure followed by friction stir processing, Mater. Sci. Eng., A, 556 (2012), 114-121.
[23] Chunjie Huang, Wenya Li, Zhihan Zhang, Maosen Fu, Marie-pierre Planche, Hanlin Liao, Ghislain Montavon, Modification of a cold sprayed SiCp/Al5056 composite coating by friction stir processing, Surf. Coat. Technol., 296 (2016), 69-75.
[24] Chunjie Huang, Wenya Li, Zhihan Zhang, Marie-pierre Planche, Hanlin Liao, Ghislain Montavon, Effect of tool rotation speed on microstructure and microhardness of friction-stir-processed cold-sprayed SiCp/Al5056 composite coating, J. Therm. Spray Technol., 25 (2016), 1357-1364.
[25] Xiao Peng Li, Gang Ji, Z Chen, Ahmed Addad, Y Wu, HW Wang, Jef Vleugels, Jan Van Humbeeck, Jean-Pierre Kruth, Selective laser melting of nano-TiB2 decorated AlSi10Mg alloy with high fracture strength and ductility, Acta Mater., 129 (2017), 183-193.
[26] Xinliang Xie, Yu Ma, Chaoyue Chen, Gang Ji, Christophe Verdy, Hongjian Wu, Zhe Chen, Sheng Yuan, Bernard Normand, Shuo Yin, Cold spray additive manufacturing of metal matrix composites (MMCs) using a novel nano-TiB2-reinforced 7075Al powder, J. Alloys Compd., 819 (2020), 152962.
[27] Rajiv S Mishra, ZY Ma, Friction stir welding and processing, Mater. Sci. Eng., R, 50 (2005), 1-78.

[28] Zhiying Liu, Hongze Wang, Michel Haché, Eric Irissou, Yu Zou, Formation of refined grains below 10 nm in size and nanoscale interlocking in the particle–particle interfacial regions of cold sprayed pure aluminum, Scripta Mater., 177 (2020), 96-100.
[29] Yu Zou, Wen Qin, Eric Irissou, Jean-Gabriel Legoux, Stephen Yue, Jerzy A Szpunar, Dynamic recrystallization in the particle/particle interfacial region of cold-sprayed nickel coating: electron backscatter diffraction characterization, Scripta Mater., 61 (2009), 899-902.
[30] P Cavaliere, A Perrone, A Silvello, Mechanical and microstructural behavior of nanocomposites produced via cold spray, Composites Part B, 67 (2014), 326-331.
[31] R Darzi Bourkhani, AR Eivani, HR Nateghi, Through-thickness inhomogeneity in microstructure and tensile properties and tribological performance of friction stir processed AA1050-Al2O3 nanocomposite, Composites Part B, 174 (2019), 107061.
[32] S Gopalakrishnan, N Murugan, Production and wear characterisation of AA 6061 matrix titanium carbide particulate reinforced composite by enhanced stir casting method, Composites Part B, 43 (2012), 302-308.
[33] Paul L Schaffer, David N Miller, Arne K Dahle, Crystallography of engulfed and pushed TiB2 particles in aluminium, Scripta Mater., 57 (2007), 1129-1132.
[34] Yu Ma, Ahmed Addad, Gang Ji, Ming-Xing Zhang, Williams Lefebvre, Zhe Chen, Vincent Ji, Atomic-scale investigation of the interface precipitation in a TiB2 nanoparticles reinforced Al–Zn–Mg–Cu matrix composite, Acta Mater., 185 (2020), 287-299.
[35] Krystian Zyguła, Bartłomiej Nosek, Hubert Pasiowiec, Norbert Szysiak, Mechanical properties and microstructure of AlSi10Mg alloy obtained by casting and SLM technique, World Scientific News, 104 (2018), 462-472.
[36] Ying-Kang Wei, Xiao-Tao Luo, Xin Chu, Guo-Sheng Huang, Chang-Jiu Li, Solid-state additive manufacturing high performance aluminum alloy 6061 enabled by an in-situ micro-forging assisted cold spray, Mater. Sci. Eng., A, 776 (2020), 139024.
[37] Xiang Qiu, Lu Qi, Ji-Qiang Wang, Tian-Ying Xiong, A hybrid approach to improve microstructure and mechanical properties of cold spray additively manufactured A380 aluminum composites, Mater. Sci. Eng., A, 772 (2020), 138828.
[38] L Gyansah, NH Tariq, JR Tang, X Qiu, JZ Gao, JQ Wang, TY Xiong, Materials Science Forum, Trans Tech Publ, 2018, pp. 62-75.
[39] NH Tariq, L Gyansah, X Qiu, H Du, JQ Wang, B Feng, DS Yan, TY Xiong, Thermo-mechanical post-treatment: A strategic approach to improve microstructure

and mechanical properties of cold spray additively manufactured composites, Mater. Des., 156 (2018), 287-299.
[40] Xiang Qiu, Lu Qi, Yu-ning Zan, Yu-jiang Wang, Ji-qiang Wang, Hao Du, Tian-ying Xiong, In-situ Sip/A380 alloy nano/micro composite formation through cold spray additive manufacturing and subsequent hot rolling treatment: Microstructure and mechanical properties, J. Alloys Compd., 780 (2019), 597-606.
[41] Mehdi Rahimian, Nader Parvin, Naser Ehsani, Investigation of particle size and amount of alumina on microstructure and mechanical properties of Al matrix composite made by powder metallurgy, Mater. Sci. Eng., A, 527 (2010), 1031-1038.
[42] C Saravanan, K Subramanian, V Ananda Krishnan, R Sankara Narayanan, Effect of particulate reinforced aluminium metal matrix composite–a review, Mechanics and Mechanical Engineering, 19 (2015), 23-30.
[43] HB Michael Rajan, I Dinaharan, S Ramabalan, ET Akinlabi, Influence of friction stir processing on microstructure and properties of AA7075/TiB2 in situ composite, J. Alloys Compd., 657 (2016), 250-260.
[44] G Liu, GJ Zhang, F Jiang, XD Ding, YJ Sun, J Sun, E Ma, Nanostructured high-strength molybdenum alloys with unprecedented tensile ductility, Nature materials, 12 (2013), 344-350.
[45] He Li, Xiaoming Wang, Lihua Chai, Haijing Wang, Ziyong Chen, Zhilei Xiang, Tounan Jin, Microstructure and mechanical properties of an in-situ TiB2/Al-Zn-Mg-Cu-Zr composite fabricated by Melt-SHS process, Mater. Sci. Eng., A, 720 (2018), 60-68.
[46] I Gutierrez-Urrutia, MA Munoz-Morris, David G Morris, Contribution of microstructural parameters to strengthening in an ultrafine-grained Al–7% Si alloy processed by severe deformation, Acta Mater., 55 (2007), 1319-1330.
[47] VC Nardone, KM Prewo, On the strength of discontinuous silicon carbide reinforced aluminum composites, Scripta Metallurgica, 20 (1986), 43-48.
[48] Ranjit Bauri, Devinder Yadav, CN Shyam Kumar, B Balaji, Tungsten particle reinforced Al 5083 composite with high strength and ductility, Mater. Sci. Eng., A, 620 (2015), 67-75.
[49] Dongshuai Zhou, Feng Qiu, Qichuan Jiang, The nano-sized TiC particle reinforced Al–Cu matrix composite with superior tensile ductility, Mater. Sci. Eng., A, 622 (2015), 189-193.
[50] Gaohui Wu, Xi Wang, Longtao Jiang, Boran Ma, A nanostructural design to

produce high ductility of high volume fraction SiCp/Al composites with enhanced strength, Mater. Des., 61 (2014), 141-145.
[51] Dongshuai Zhou, Feng Qiu, Qichuan Jiang, Simultaneously increasing the strength and ductility of nano-sized TiN particle reinforced Al–Cu matrix composites, Mater. Sci. Eng., A, 596 (2014), 98-102.